A multiscale methodology for small-scale bubble dynamics in turbulence

Citation for the original published paper (version of record):
Hidman, N., Ström, H., Sasic, S. et al (2022). A multiscale methodology for small-scale bubble dynamics in turbulence. International Journal of Multiphase Flow, 150.
http://dx.doi.org/10.1016/j.ijmultiphaseflow.2022.103976

International Journal of Multiphase Flow 150 (2022) 103976

Contents lists available at ScienceDirect

International Journal of Multiphase Flow

journal homepage: www.elsevier.com/locate/ijmulflow

A multiscale methodology for small-scale bubble dynamics in turbulence

Niklas Hidman *, Henrik Ström, Srdjan Sasic, Gaetano Sardina

Department of Mechanical and Maritime Sciences, Chalmers University of Technology, Gothenburg, Sweden

ARTICLE INFO

Keywords:
Bubbles
Turbulence
Multiscale method
Moving reference frame
DNS

ABSTRACT

We formulate in this paper a multiscale numerical framework that handles small-scale bubble dynamics in turbulence. Our framework involves bubbles with arbitrary density ratios with the carrier phase. We use a Moving Reference Frame method that follows a bubble to deal with a fast rising of bubbles present at high density ratios between the phases. We use a Proportional Integral Derivative controller to handle an additional acceleration term in the governing equations that stems from the change of a coordinate system from a fixed to a non-inertial one. Our framework accounts for the fact that the dynamics of bubbles are significantly influenced by the unsteadiness of the small-scale turbulent liquid fluctuations that modify the bubble shapes and alter their motion. In addition, we improve and speed up, with at least two orders of magnitude in computational time, the numerical framework recently proposed by Milan et al. (2020). The developed numerical framework can capture processes occurring at time scales even smaller than the Kolmogorov times. It can be applied to droplets, bubbles or particle systems in both laminar and turbulent flows, using any general DNS technique that handles two-phase flows.

1. Introduction

Predicting the dynamics of bubbly flows is still an unsolved problem in fluid mechanics (Magnaudet and Eames, 2000) even in the absence of phase transitions. The main challenges are due to their multiscale nature, where the phenomenologies occurring at the smallest scales of the order of a bubble diameter (micro-/millimeters) affect the macroscales of the order of an industrial apparatus (meters) and vice versa. This huge scale separation cannot be captured even with the most advanced experimental or numerical techniques. Consequently, the design and scale-up of large industrial systems like bubble column reactors are extraordinarily complicated and based on empirical correlations (Conesa, 2019).

The classic modeling approach in multiphase flows is based on a bottom-up hierarchical strategy (van der Hoef et al., 2008) to parametrize the physical phenomenologies occurring at different length scales starting from the small to the large scales of the system using different and separate approaches. In particular, the small-scale simulations resolve the dynamics and deformation of every single bubble in an Eulerian grid (bubble-resolved DNS) (Bunner and Tryggvason, 1999; Dijkhuizen et al., 2010; Tripathi et al., 2014; Cano-Lozano et al., 2016) in simple steady configurations such as quiescent or linear shear flows. This microscopic approach (grid size much smaller than the bubble diameter) requires a high computational cost, and for this reason, only domains of the order of several bubble diameters can be simulated.

The main objective of the microscopic approach is to increase our physical understanding and to formulate empirical models, e.g. interfacial force coefficients, breakup and coalescence criteria, bubble shape and deformation characteristics, that can be used for larger-scale simulation approaches like Eulerian–Lagrangian (EL) or Eulerian–Eulerian (EE) frameworks (Delnoij et al., 1999; Ferrante and Elghobashi, 2004; Sardina et al., 2019; Jareteg et al., 2017; Panicker et al., 2020). However, the bottom-up hierarchical modeling strategy does not consider the complex multiscale coupling that exists in multiphase flows. The small-scale dynamics cannot be approximated as a steady flow since, in reality, unsteady intermittent turbulent fluctuations are still present even at the smallest turbulent scales (Kolmogorov scale) and affect the bubble shape, deformation and dynamics. Given the current computational limitations, there is a need to develop such numerical methodologies where the bubbles are subjected to realistic turbulent fluctuations and shear rates, while preserving the ability of the framework to fully resolve bubble deformation occurring at scales smaller than their diameter.

Recently, Milan et al. (2020) developed a multiscale approach to study droplet dynamics and deformation in isotropic turbulence when the droplet diameter is of the same order or smaller than the smallest turbulent length scale. In particular, their methodology computes an unsteady external flow field via a pseudo-spectral simulation, describing the trajectory of a passive tracer in isotropic turbulence, and use

* Corresponding author.
E-mail address: niklas.hidman@chalmers.se (N. Hidman).

https://doi.org/10.1016/j.ijmultiphaseflow.2022.103976
Received 28 June 2021; Received in revised form 26 November 2021; Accepted 13 January 2022
Available online 31 January 2022

this external flow as boundary conditions in a Lattice-Boltzmann solver containing a single droplet. In this way, the microscopic scale dynamics of the droplet are coupled with the macroscopic properties of the underlying turbulent flow. Their results show an excellent agreement between the predicted droplet deformation and previous theoretical models. This work constitutes a first fundamental step towards coupled multiscale simulations of multiphase flows. Nevertheless, the approach has two constraints: (1) the turbulent signals extracted following a passive tracer are different from the ones calculated following rising bubbles or falling droplets at finite relaxation times, since these objects tend to preferentially sample high-vorticity (bubbles) or high-strain rate (droplets) regions (Toschi and Bodenschatz, 2009), (2) the droplet and the carrier fluid share the same density. While the first issue can be trivially fixed by extracting the turbulent velocity and shear rates following a Lagrangian bubble or droplet, the second one regarding density ratios larger or smaller than unity and the consequent effect of gravity is a considerable challenge to the development of a general multiscale approach.

For example, rising bubbles exhibit a fascinating variety of trajectory behaviors, some of which develop over relatively long spatial and temporal scales. (Cano-Lozano et al., 2016) performed DNS simulations of the rise of a single bubble in a quiescent liquid and classified bubble motions into rectilinear, zigzagging, spiraling and chaotic regimes depending on the problem parameters. For the bubble path to develop into those regimes, the required size of the computational domain was at least 128 bubble diameters. The presence of shear in the continuous phase introduces additional requirements in the computational domain. Since the shear flow field advects the bubble, the latter travels further in the transversal direction than does a corresponding bubble in a quiescent liquid, reaching the lateral boundaries of the domain. The required domain size is challenging to determine a priori and leads to unfeasible DNS simulations in case of fast-rising bubbles (excessive vertical lengths) or high-shear flows (excessive transversal lengths). Moreover, the initial domain size is problematic to select if we want to investigate the breakup process where the breakup location and time are unknown.

In this work, we extend the multiscale approach by Milan et al. (2020) to bubbles with arbitrary density ratios between the phases (our methodology can also be applied to arbitrary density droplets). In particular, the challenge induced by a different density ratio and coupled with the presence of the gravitational force has been solved by adopting a change of a coordinate system to a frame moving one with a bubble. The same change of coordinates was used in the seminal paper by Maxey and Riley (1983) to analytically derive the equation of motion of a rigid particle in Stokes flow.

The change of the coordinate system into a moving reference frame (MRF) introduces an additional acceleration term in the Navier–Stokes equations that is proportional to the bubble acceleration. The MRF technique can be implemented in different ways, for example, following a single bubble or droplet by updating the velocity of the MRF using the particle volume-averaged velocity (Lörstad and Fuchs, 2004; Lörstad et al., 2004). Also Rusche (2002) studied the dynamics of a single bubble using a reference frame moving with the bubble. The velocity of that MRF was updated based on the bubble displacement from its initial relative position combined with relaxation factors.

Updating the velocity of the MRF with the bubble velocity introduces a numerical drift of the bubble from its initial position. The reason is that an explicit update of the MRF velocity introduces a small difference between the bubble and MRF velocities that results in a bubble displacement that accumulates over time. Moreover, updating the MRF velocity based on the bubble displacement may cause highly varying and even unstable velocity corrections during high bubble accelerations. A different approach was used by Fan et al. (2021) and Kekesi et al. (2016) that studied bubble and droplet deformation and breakup dynamics using DNS simulations and kept the fluid particle in the center of the domain by applying an artificial body force on the particle. In the former study, a Proportional Integral Derivative (PID)-controller was used to specify the body force. The body force acts on the dispersed phase and balances the drag and lift forces induced by the flow, thus keeping the moving object stationary in the domain.

We succeeded to combine the MRF technique and the PID-controller approach into a numerical method that allows for efficient multiscale DNS simulations in the reference frame of the bubbles. This method reduces the required size of the computational domain and thus reduces the computational cost. In our method, we employ a PID-controller, but instead of applying an artificial force on the bubbles, we uniformly accelerate the entire computational domain so that the domain follows the motion of the bubbles. The PID controller determines the MRF acceleration based on the bubble displacement (in the P and I parts) and the relative bubble velocity (in the D part). This approach gives superior performances in minimizing artificial numerical drifts even in the presence of large bubble accelerations induced by the external turbulent flow.

In addition, we have increased the computational speed of the methodology of Milan et al. (2020) by at least two orders of magnitude, using additional body forces proportional to the time derivatives of the boundary conditions and avoiding computationally expensive sub-iterations in the algorithm.

A detailed description of the modeling setup, assumptions and numerical algorithm is provided in Section 2. The multiscale approach for single-phase flows is validated in Section 3.1, while the ability of the PID-controller and the MRF technique to correctly describe the dynamics of rising bubbles in simple laminar flows and in a number of situations (e.g. coalescence and breakup of bubbles) is evaluated in Sections 3.2–3.4 and in Appendix B. Section 3.5 describes the motion of a deformable bubble in a turbulent flow field and, finally, Section 4 presents the conclusions.

2. Description of the numerical framework

Our methodology couples two fluid dynamics solvers. In particular, we study the detailed dynamics and deformation of bubbles at the microscale using a Volume of Fluid (VOF) solver with unsteady boundary conditions sampled from a Lagrangian bubble trajectory in an external turbulent field. This multiscale coupling can capture the large-scale characteristics of turbulence and simulate a more realistic flow around the bubble whose size is comparable to or smaller than the Kolmogorov scale $\eta = (\nu^3/\varepsilon)^{1/4}$, where ν is the liquid kinematic viscosity and ε is the turbulent kinetic energy dissipation rate. A simple illustration of the algorithm is presented in Fig. 1 where an instantaneous vorticity field of the macroscale simulation is plotted on the left side. In the same figure, the right side shows an instantaneous configuration of a deformed rising bubble in the microscale framework. The turbulent macroscale vorticity field has been obtained using a pseudo-spectral Eulerian–Lagrangian solver. The microscale VOF result includes the streamlines of the flow field surrounding the particle with contours proportional to the intensity of the vorticity vector. The two different solvers and the coupling algorithms are presented in the following two sections.

2.1. Macroscale framework–Eulerian-Lagrangian (EL) solver and generation of the external turbulent flow

The external turbulent flow (or macroscale flow) is generated using a pseudospectral solver that simulates homogeneous isotropic turbulence. Assuming a low bubble volume fraction, the liquid velocity satisfies the standard incompressible Navier–Stokes equations:

$$\frac{\partial u_i^e}{\partial x_i^e} = 0\,, \tag{1}$$

$$\frac{Du_i^e}{Dt} = \frac{\partial u_i^e}{\partial t} + u_j^e \frac{\partial u_i^e}{\partial x_j^e} = -\frac{1}{\rho}\frac{\partial p^e}{\partial x_i^e} + \nu \frac{\partial^2 u_i^e}{\partial x_j^e \partial x_j^e} + f_i \tag{2}$$

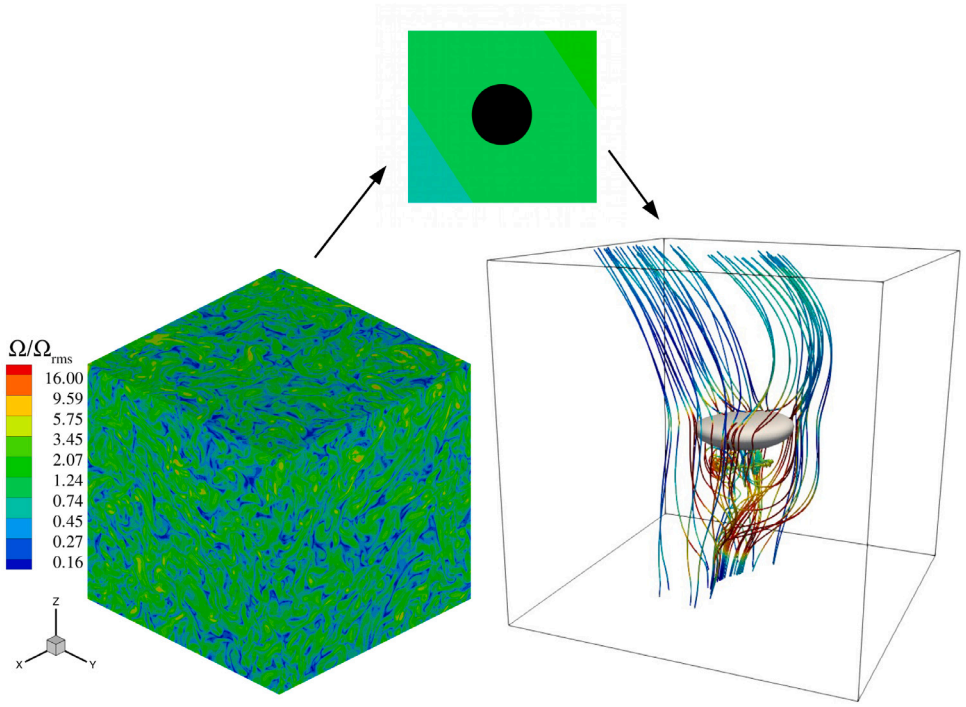

Fig. 1. Simplified sketch of the multiscale approach with instantaneous configurations of the macroscale (left side) and the microscale (right side) frameworks. The two solvers are coupled with the turbulent flow field characteristics extracted in the macroscale simulation following a spherical Lagrangian bubble (center). The contour levels of all subfigures are proportional to the magnitude of the liquid vorticity.

where t and x_i^e indicate the time and the spatial coordinate vector, u_i^e and p^e are the external liquid velocity and pressure, ρ is the liquid density, and f_i is a random forcing field necessary to maintain the turbulent velocity in a statistically steady state. We assume periodic boundary conditions in the three directions and a cubic computational domain. The equation system (1)–(2) is solved in the Fourier space employing a fast Fourier transform. The nonlinear terms are evaluated in physical space using the classic 2/3 rule to avoid any aliasing error. Time integration is performed with a third-order, low-storage Runge–Kutta method where the diffusive terms are analytically calculated while an Adam–Bashforth scheme is employed for the nonlinear terms. The stochastic forcing is evaluated in the Fourier space and acts isotropically on the first shell of wave vectors. The forcing amplitude is constant and the field is delta-correlated in time and uniformly distributed in phase and directions. The bubbles are evolved in a Lagrangian framework and are subjected to the following forces: added mass, pressure gradient, drag, buoyancy, gravity and lift. The bubble equation of motion reads:

$$\frac{dx_i^b}{dt} = v_i^b, \tag{3}$$

$$\frac{dv_i^b}{dt} = \beta\frac{Du_i^e}{Dt} + \frac{u_i^e - v_i^b}{\tau_b} f(Re_b) + (1-\beta)g\delta_{i3} - \epsilon_{ijk}(v_j^b - u_j^e)\omega_k, \tag{4}$$

where x_i^b is the bubble position, $\beta = 3\rho/(\rho + 2\rho_b)$ is the density ratio with ρ_b the bubble density, $\tau_b = d_b^2/8\nu\beta$ is the bubble relaxation time where d_b is the bubble diameter, $f(Re_b)$ a nonlinear drag coefficient depending on the bubble Reynolds number $Re_b = |u_i - v_i^b|d_b/\nu$, g the gravitational acceleration, δ and ϵ are the Kronecker delta and Levi-Civita symbols, ω is the fluid vorticity at the particle position. The nonlinear correction for the drag is given by the following expression:

$$f(Re_b) = 1 + \frac{Re_b}{8 + \frac{1}{2}\left(Re_b + 3.315\sqrt{Re_b}\right)}, \tag{5}$$

found by Mei and Klausner (1992) and employed in Spandan et al. (2016). We assume the added mass and the lift coefficient equal to 0.5. The same Runge–Kutta scheme employed for the Eulerian solver is used to integrate the bubble equation of motion. The liquid velocity and vorticity components at the bubble positions are calculated with a second-order interpolation scheme. The same interpolation scheme is employed to extract the unsteady liquid velocities $u_i^{e,b}(t)$ and velocity gradients $\partial u_i^{e,b}/\partial x_j^e(t)$ along the bubble trajectory that will be used as boundary conditions for the microscopic approach. The spatial resolution of the liquid phase must be fine enough to capture even the flow velocity gradients. More numerical details on the Eulerian–Lagrangian (EL) solver can be found in Sardina et al. (2015) for droplet-laden and Sardina et al. (2019) for bubble-laden flows.

2.2. Microscale framework–volume of fluid solver in the MRF

To solve the microscale multiphase problem, we employ the Volume of Fluid (VOF) numerical approach. In this framework, the position of the two phases is tracked using a volume fraction field c. The volume fraction field is either one if the phase is present or zero if the other phase is. The governing equations are the incompressible Navier–Stokes equations together with the advection of the volume fraction according to

$$\frac{\partial u_i}{\partial x_i} = 0\,, \tag{6}$$

$$\rho\left(\frac{\partial u_i}{\partial t} + u_j\frac{\partial u_i}{\partial x_j}\right) = \rho g_i - \frac{\partial p}{\partial x_i} + \frac{\partial}{\partial x_j}\left(\mu\left(\frac{\partial u_i}{\partial x_j} + \frac{\partial u_j}{\partial x_i}\right)\right) + \sigma\kappa\delta_S n_i\,, \tag{7}$$

$$\frac{\partial c}{\partial t} + \frac{\partial (cu_i)}{\partial x_i} = 0 \tag{8}$$

where u_i and g_i are the microscale fluid velocity and gravitational acceleration, σ is the surface tension, δ_S is the Dirac distribution function that localizes the surface tension term at the interface and κ and n_i are the curvature and the normal vector of the interface. The density ρ and viscosity μ are defined as

$$\rho(c) = c\rho_l + (1-c)\rho_g\,, \tag{9}$$

$$\mu(c) = \left(\frac{c}{\mu_l} + \frac{1-c}{\mu_g} \right)^{-1} \tag{10}$$

where the symbols l and g indicate the liquid and the gas phases. The viscosity is computed using a harmonic mean that is in general more accurate for interfaces with a continuous shear stress that we aim at resolving with the current framework (Tryggvason et al., 2011).

In this work, we mostly focus on a single bubble rising in a liquid. This problem is completely described by the following four dimensionless parameters (Tripathi et al., 2014): the Galilei number $Ga = \rho_l \sqrt{gD} D/\mu_l$ that relates buoyancy to viscous forces, the Eötvös number $Eo = \rho_l g D^2/\sigma$ that relates buoyancy to surface tension forces, the density ratio $\rho_r = \rho_l/\rho_g$ and the dynamic viscosity ratio $\mu_r = \mu_l/\mu_g$. Here, D is the spherical equivalent bubble diameter and for all cases in this paper (unless otherwise stated) we use the density and viscosity ratios of $\rho_r = 1000$ and $\mu_r = 100$ that are similar to a water-air system. If the bubble is rising in a shear liquid flow, also the dimensionless shear rate is introduced $Sr = \frac{\omega D}{\sqrt{gD}}$, where ω is the shear rate of the surrounding liquid flow. In the remainder of this work (unless otherwise stated), all variables are made non-dimensional by the diameter D, gravitational acceleration g, the surrounding liquid density ρ_l and the liquid viscosity μ_l: $x_i^* = x_i/D$, $u_i^* = u_i/\sqrt{gD}$, $t^* = t/\sqrt{D/g}$, $\rho^* = \rho/\rho_l$, $\mu^* = \mu/\mu_l$, $p^* = p/(\rho_l g D)$, $g_i^* = g_i/g$ and $\kappa^* = \kappa D$.

2.3. Non-inertial Moving Reference Frame (MRF)

To solve the problem in a reference frame that moves with the bubble, we make the following change of variables:

$$\hat{x}_i^* = x_i^* - x_{mrf,i}^*, \tag{11}$$

$$\hat{u}_i^* = u_i^* - u_{mrf,i}^*, \tag{12}$$

$$\hat{t}^* = t^* \tag{13}$$

where $\hat{x}_i^*$ represents the non-dimensional relative position in the MRF and $\hat{u}_i^*$ is the relative velocity within the MRF, $x_{mrf,i}^*$ and $u_{mrf,i}^*$ are the absolute position and velocity of the MRF. An illustration of the coordinate systems is shown in Fig. 2. Omitting the asterisks, the non-dimensional governing equations for the flow in the MRF become:

$$\frac{\partial \hat{u}_i}{\partial \hat{x}_i} = 0, \tag{14}$$

$$\rho \left(\frac{\partial \hat{u}_i}{\partial \hat{t}} + \hat{u}_j \frac{\partial \hat{u}_i}{\partial \hat{x}_j} \right) = \rho \left(g_i - a_{mrf,i} \right) - \frac{\partial p}{\partial \hat{x}_i} + \frac{1}{Ga} \frac{\partial}{\partial \hat{x}_j} \left(\mu \left(\frac{\partial \hat{u}_i}{\partial \hat{x}_j} + \frac{\partial \hat{u}_j}{\partial \hat{x}_i} \right) \right) + \frac{\hat{\kappa} \delta_S \hat{n}_i}{Eo}, \tag{15}$$

$$\frac{\partial c}{\partial \hat{t}} + \frac{\partial c \hat{u}_i}{\partial \hat{x}_i} = 0, \tag{16}$$

with the notable addition of the term representing the acceleration of the MRF in the momentum Eq. (15). For an equal density case between the two phases as in Milan et al. (2020), the additional acceleration term can be included in a modified pressure term because the momentum equations are invariant under rectilinear acceleration of the frame (extended Galilean invariance, Pope (2001)).

This system of partial differential equations is solved using the open-source code Basilisk on cell-centered Cartesian grids with the option to use a tree-based adaptive grid refinement technique (Popinet, 2015). A time-splitting projection method is used with standard, second-order, numerical schemes for the spatial gradients, and the velocity advection term is estimated with the Bell–Colella–Glaz second-order unsplit upwind scheme (Popinet, 2003). With this approach, the problem is reduced to a Helmholtz–Poisson equation for the pressure and the velocity components and a Poisson problem for the pressure correction. These equations are solved using a multilevel solver on the tree-based grid-structure. A second-order staggered discretization in time is used for the scalar and velocity fields so that the velocity is computed at time $n+1$ and the scalar fields at $n+1/2$. The advection of the volume fraction is achieved with the Volume of Fluid piecewise-linear interface reconstruction method that, at each computational time step and a cell containing the interface, reconstructs the advected interface by a line in 2D or a plane in 3D (Scardovelli and Zaleski, 1999). The advection of the volume fraction is then performed with a geometrical flux estimation based on the reconstructed interface (Popinet, 2015). Because of the reconstruction, a sharp interface is maintained throughout the simulations. The surface tension term is handled using a balanced-force approach that ensures that the pressure gradient and volume fraction gradients are discretized consistently. The interface curvature is estimated using a generalized height-function method in cell stencils at the interface (Popinet, 2015) that provides accurate estimates of the curvature.

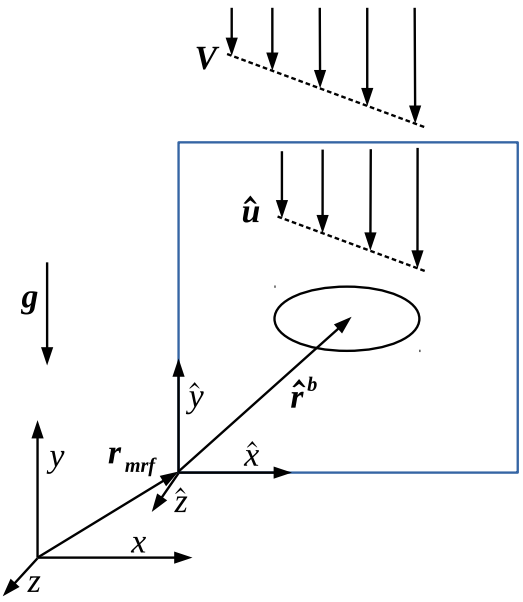

Fig. 2. Illustration of the moving reference frame with the centered bubble and the absolute and relative coordinate systems. The $\hat{x}_i$ and $\hat{u}_i$ represent the spatial coordinates and velocity field in the MRF. The external velocity field V_i is defined in an absolute reference frame and this field is imposed on the MRF as described in Section 2.5.

2.4. PID-controller

The aim of the MRF is to keep the bubble at its initial relative position. This can be achieved in several ways. In this work, the acceleration of the MRF is updated at every time step using a PID-controller where the error value e_i is the distance between the bubble relative center of mass $\hat{x}_i^{n,b}$ and its initial relative position $\hat{x}_i^{0,b}$. The error in the derivative part $\frac{de_i^n}{dt}$ is thus the relative velocity of the bubble. The MRF acceleration and velocity are determined as

$$a_{mrf,i}^{n+1} = K_{P,i} \left(e_i^n + \frac{1}{T_{I,i}} \int_0^{t^n} e_i(t')dt' + T_{D,i} \frac{de_i^n}{dt} \right), \tag{17}$$

$$u_{mrf,i}^{n+1} = u_{mrf,i}^n + a_{mrf,i}^{n+1} \Delta t, \tag{18}$$

$$e_i^n = \hat{x}_i^{n,b} - \hat{x}_i^{0,b}, \tag{19}$$

where $K_{P,i}$, $T_{I,i}$ and $T_{D,i}$ are the ith component of the proportional, integral and derivative coefficients, respectively. In this work, the heuristic, and systematic, Ziegler–Nichols (Ziegler et al., 1942) tuning method is used to obtain the coefficients. Generally, the method starts by setting the proportional, integral and derivative gains to zero ($K_{P,0} = 0, T_{I,0} = \infty, T_{D,0} = 0$). Then, the proportional gain K_P is increased until an ultimate gain K_U is reached where the output signal $a_{mrf}(t)$ displays stable and consistent oscillations. The oscillation period is

defined as T_U and, together with K_U, these parameters determine appropriate coefficients according to $K_P = K_U/3, T_I = T_U/2, T_D = T_U/3$ (McCormack and Godfrey, 1998).

Instead of starting from $K_{P,0} = 0$ in the Ziegler–Nichols method, we determine an approximate value for K_P used as an improved starting point. For this estimation, we assume that the maximum necessary output signal is the bubble acceleration just after initialization, $\max(a_{mrf}(t)) \approx a_B(t = 0^+)$. At this instant, the relative velocity is almost zero so that the buoyancy and added mass forces govern the bubble acceleration. For bubbles, the density ratio $\rho_r \gg 1$ and the added mass coefficient $c_{AM} = 1/2$ give $a_B(t = 0^+) \approx 2g$ (for droplets $\rho_r \ll 1$ and $a_B(t = 0^+) \approx g$). Neglecting the integral and derivative parts by setting $T_{I,i} = \infty$, $T_{D,i} = 0$ and $a_{mrf} = a_B$ in Eq. (17), gives $K_{P,i} = a_B/e_i$.

Even during the high initial bubble acceleration we want the bubble displacement $e_i < (D/100)$. For bubbles, a reasonable starting point then becomes $K_{P,0} > 2g/(D/100)$ and for droplets $K_{P,0} > g/(D/100)$. In this work, we study bubbles with $D = g = 1$ (in nondimensional units) which gives $K_{P,0} \sim 200$ as a reasonable starting point. Using this starting point in the Ziegler–Nichols method, we got the parameters ($K_{P,i} = 330$, $T_{I,i} = 0.2$ and $T_{D,i} = 0.13$) that gave stable regulations and small bubble displacements for all our simulation cases in both 2D and 3D.

Alternatively, the PID-controller can calculate a correction to the MRF velocity $u^{n+1}_{mrf,corr,i}$ so that the updated velocity is $u^{n+1}_{mrf,i} = u^n_{mrf,i} + u^{n+1}_{mrf,corr,i}$. With this approach, the acceleration of the MRF becomes $a^{n+1}_{mrf,i} = u^{n+1}_{mrf,corr,i}/\Delta t$. Thus, the MRF acceleration becomes large for the cases where the correction velocity is large and, especially, the variable time step size Δt is small. The velocity-correction approach was also tested and, indeed, gave less stable regulations for the cases where the time step size varied significantly. The proposed acceleration-based method in Eqs. (17) and (18) ensures that the change of the MRF velocity $(u^{n+1}_{mrf,i} - u^n_{mrf,i}) \to 0$ when $\Delta t \to 0$. This property provides a smooth acceleration of the MRF and hence a smooth acceleration of the velocity field $\hat{u}_i$ inside the domain. The same property does not hold for the velocity-correction method which can potentially result in highly varying accelerations between discrete time steps. In all the cases in this work we employ the acceleration-based method.

2.5. Imposing external velocity field and boundary conditions

The velocity of the MRF is updated at every time step by uniformly applying the MRF acceleration from Eq. (17) into the momentum Eq. (15) and by updating all Dirichlet velocity conditions at the inlet boundaries as

$$\hat{u}_{BC,i}(\hat{x}_j, t) = V^{(1)}_i(\hat{x}_j, t) - u_{mrf,i}(t)\,, \tag{20}$$

where $V^{(1)}_i$ is the linearized external liquid flow field.

The coupled algorithm uses the unsteady liquid velocity and gradient tensor at the bubble position extracted from the macroscale simulations as boundary conditions in the microscale VOF solver. The liquid velocity at the bubble position in the macroscale simulations can be evaluated using an interpolation scheme along the bubble trajectory for dilute suspensions (one-way coupling). For dense suspensions (two-/four-way coupling), the evaluation is slightly more complex because the feedback force induced by each bubble to the carrier phase modifies the flow, generating a self-induced velocity disturbance. The undisturbed velocity along the bubble trajectory must be corrected by removing the self-induced disturbance generated by the bubble itself, and several algorithms have been developed in the last decade addressing this specific question (Gualtieri et al., 2015; Horwitz and Mani, 2018; Balachandar et al., 2019; Evrard et al., 2020).

For length scales comparable to the Kolmogorov scale, the liquid velocity field surrounding the bubble can be approximated as a linear function of the spatial coordinate (Pope, 2001) since the velocity increments $\delta u_i(x_i, r_i) = u_i(x_i + r_i) - u_i(x_i) \propto r_i$, where r_i is the distance between two points. Using Taylor's expansion, this flow field is expressed as:

$$V^{(1)}_i(\hat{x}_i, t) = u^{e,b}_i(t) + \frac{\partial u^{e,b}_i}{\partial \hat{x}_j}(t)(\hat{x}_j - \hat{x}^b_j)\,, \tag{21}$$

where $u^{e,b}_i(t)$ and $\dfrac{\partial u^{e,b}_i}{\partial \hat{x}_j}(t)$ are the absolute velocity and gradients, respectively, of the liquid velocity field at the bubble position and time t extracted from the macroscale simulations. We impose $V^{(1)}_i$ as an undisturbed velocity field in the microscopic solver and, in this context, this velocity field is denoted the external flow field. We remark that Eq. (21) is valid for computational domain lengths in the microscale simulations that are comparable with the viscous scale of the flow.

If the external flow field is indeed unsteady, i.e. accelerating, the flow field in the MRF should be accelerated correspondingly. Therefore, additional non-uniform acceleration source terms are introduced into the momentum Eq. (15) according to

$$a^{(1)}_{V,i}(\hat{x}_i, t) = \frac{d}{dt}(u^{e,b}_i) + \frac{d}{dt}\left(\frac{\partial u^{e,b}_i}{\partial \hat{x}_j}\right)(\hat{x}_j - \hat{x}^b_j)\,. \tag{22}$$

The MRF computational domain is outlined in Fig. 2 and constitutes a box in 3D with gravity acting in the negative y-direction. The domain boundary conditions are specified in Table 1 where the hydrostatic pressure field is imposed on the domain. The lateral boundaries switch between inlet and outlet boundary conditions depending on the normal relative velocity direction at the boundary according to Eq. (20).

The position of the MRF and the absolute position and velocity of the bubble are evaluated by

$$x^{n+1}_{mrf,i} = x^n_{mrf,i} + \frac{1}{2}(u^{n+1}_{mrf,i} + u^n_{mrf,i})\Delta t\,, \tag{23}$$

$$x^{n,b}_i = x^n_{mrf,i} + \hat{x}^{n,b}_i\,, \tag{24}$$

$$u^{n,b}_i = u^n_{mrf,i} + \hat{u}^{n,b}_i\,, \tag{25}$$

where the bubble relative position and velocity are determined from

$$m^b = \int_\Omega (1 - c)\rho d\Omega\,, \tag{26}$$

$$\hat{x}^b_i = \frac{1}{m^b}\int_\Omega (1 - c)\hat{x}_i \rho d\Omega\,, \tag{27}$$

$$\hat{u}^b_i = \frac{1}{m^b}\int_\Omega (1 - c)\hat{u}_i \rho d\Omega\,. \tag{28}$$

Here, Ω denotes the entire computational spatial domain and m^b is the mass of the bubble. In summary, for the microscopic solver with a moving reference frame, the governing Eqs. (14)–(16) for the internal flow field are solved together with Eqs. (17)–(28) that handle the motion of the reference frame and the evolution of the external velocity field.

Table 1
Boundary conditions for the pressure and velocity components. Here, n denotes the normal direction and t the tangential directions of the specific boundary. The lateral boundaries are specified as either inlet or outlet depending on the direction of the normal relative velocity.

Boundary	Pressure	Normal velocity	Tangential velocity
Top	$\nabla_n p = -\rho_l g$	$\hat{u}_n = \hat{u}_{BC,n}$	$\nabla_t \hat{u} = \nabla_t V^{(1)}$
Bottom	$p = 0$	$\nabla_n \hat{u} = \nabla_n V^{(1)}$	$\nabla_t \hat{u} = \nabla_t V^{(1)}$
Lateral	$\nabla_n p = 0$ or $p = -\rho_l g y$	$\hat{u}_n = \hat{u}_{BC,n}$ or $\nabla_n \hat{u} = \nabla_n V^{(1)}$	$\nabla_t \hat{u} = \nabla_t V^{(1)}$

3. Validations and simulation results

3.1. Turbulent external velocity field

We first validate the coupled numerical framework by looking at a single-phase flow case. In particular, we want to show that by

extracting the unsteady velocity components and velocity gradients in the macroscale simulations, we can reproduce the linear profile (Eq. (21)) in the microscale VOF framework. The macroscale pseudo-spectral simulation corresponds to homogeneous isotropic turbulence with the Taylor Reynolds number $Re_\lambda = u_{rms}\lambda/\nu = 180$ where u_{rms} is the root mean square of the velocity fluctuations and $\lambda = \sqrt{\varepsilon/15\nu u_{rms}}$ is the Taylor length scale. We employed a resolution of 256^3 grid points in a cubic computational domain of $2\pi^3$. The non-dimensional Kolmogorov length scale is 0.015 and the Kolmogorov time is 0.35. Assuming water as a fluid and a turbulent dissipation rate of 1.5 10^{-5} m^2/s^3, the Kolmogorov scales correspond to 0.5 mm for the length and 0.26 s for the time.

In Appendix A, we show the turbulent kinetic energy and dissipation spectra from the macroscale simulation. Based on the dissipation spectrum, the spatial resolution of the macroscale simulation is sufficient to capture all relevant turbulent length scales.

We test the convergence of the microscale simulations using a similar approach as described in Milan et al. (2020), where the linear velocity profile is reproduced in the microscale simulation using unsteady boundary conditions proportional to the gradient of the velocity field of the macroscale simulation extracted along a Lagrangian trajectory. From this test, we can confirm that the coupling algorithm at the microscale recovers the turbulent velocity components and velocity gradients of the macroscale simulations. The top panel of Fig. 3 shows the time series of the modulus of the rate of the strain tensor $|S^e_{ij}| = \sqrt{S^e_{ij}S^e_{ij}}$ (S^e_{ij} is the symmetric part of the velocity gradient $\partial u^{e,b}_i/\partial\hat{x}_j$) as a function of time representing the behavior of a typical turbulent signal for the gradients with localized peaks much larger than the average value. Given the signal of $u^{e,b}_i(t)$ and $\dfrac{\partial u^{e,b}_i}{\partial\hat{x}_j}(t)$ from the macroscale simulation, the desired linear velocity field in the microscale simulation at a given time is obtained by Eq. (21).

The normalized error function between the calculated velocity field in the microscale simulation $\hat{u}_i(\hat{x}_i,t)$ and the linear field $V^{(1)}_i(\hat{x}_i,t)$ is given by:

$$E^{(1)} = \frac{1}{V^{(1)}_{rms}(t)}\sqrt{\frac{1}{L^3}\int\sum_{i=1}^{3}\left(\hat{u}_i(\hat{x}_i,t) - V^{(1)}_i(\hat{x}_i,t)\right)^2 d\hat{x}_1 d\hat{x}_2 d\hat{x}_3} \tag{29}$$

where L indicates the domain length. Since we apply an unsteady velocity boundary condition, the numerical solution at the center of the domain will not instantaneously adapt to the linear solution. However, it will require a finite convergence time until the error defined in (29) becomes sufficiently small. Milan et al. (2020) minimized the error by performing a number of finite sub-iterations for each physical time step. In particular, the number of iterations ranges between 200 and 1200 depending on the domain length to achieve a computational error smaller than 10% with a corresponding increase of the computational times. Here, we present an alternative approach to drastically speed up the run times, avoiding the need for sub-iteration by adding to the momentum equation an additional body force proportional to the time derivatives of the boundary conditions as described in Eq. (22). This algorithm is applied to a single-phase simulation with unsteady boundary conditions, a domain length of almost 16η and a numerical resolution of 64^3 equispaced computational cells. The bottom panel of Fig. 3 shows the error $E^{(1)}$ that is always less than 10% at each computational time, and, after the initial period, the error stays below 5% even during the sudden peak of $|S^e_{ij}|$ at $t/\tau_\eta \approx 3.8$. Consequently, the novel approach is at least 200 times computationally faster since it is free from additional sub-iterations.

3.2. Bubble rising rectilinearly in quiescent liquid

Before fully coupling the two frameworks for the rising bubble multiscale simulations, we validate the PID-controlled MRF approach for the microscale simulations in steady laminar flows. This step is crucial

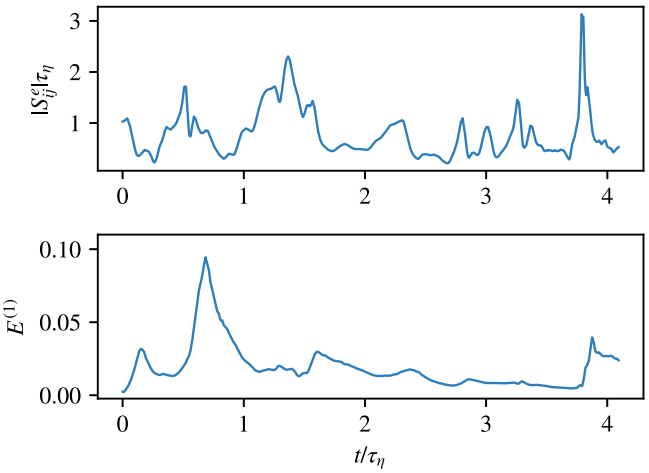

Fig. 3. Time series of the modulus of the symmetric part of the velocity gradient tensor S^e_{ij} (top panel) and the error between the numerical and linearized velocity fields (bottom panel).

when high-density contrasts between the two phases are present and large buoyancy/gravity forces induce a relative rising/sinking motion of the dispersed phase. We start to study a simple case such as the rise of a 2D bubble in a domain of $2D \times 4D$ for increasingly complex motions of the MRF in a quiescent liquid, so that $V^{(1)}_i = 0$. The bubble dynamics predicted in the different cases are compared with results from an absolute (stationary) reference frame. In the absolute reference frame, the initial bubble position is in the center of the domain and $1D$ above the bottom, while for the other reference frames, the initial position is $2D$ above the bottom. The governing parameters are $Ga = 10$ and $Eo = 1$, which results in an approximately spherical bubble. In this case, we use a uniform grid of 32 cells/D to exclude possible effects from the adaptive grid refinement technique.

MRF at constant velocity. Here we test the simplest case of a reference frame moving with a constant velocity. From the simulation with the absolute reference frame, the non-dimensional terminal velocity of the bubble is $u^b_{y,T} \approx 0.3$. To maintain the bubble close to its initial position, we specify the constant velocity of the MRF equal to the terminal velocity of the bubble. Since the MRF velocity is constant, the MRF is still an inertial reference frame where the unaltered governing Eqs. (6)–(8) are valid. The results from this simulation should therefore compare well with the simulation in the absolute reference frame. The motion of the bubble in the absolute reference frame is computed using Eqs. (23)–(25).

MRF at constant acceleration. In this case, we increase the complexity of the MRF motion by considering a non-inertial reference frame with a constant acceleration. The acceleration is chosen as the approximate average bubble acceleration until it reaches the terminal velocity according to $a^b_y = 0.1$. This value ensures that the bubble stays close to the center of the domain during the entire simulation time.

PID-controlled MRF. Finally, we let the PID-controller specify the acceleration of the MRF that aims at keeping the bubble at its initial relative position. Now, the acceleration source terms in Eq. (15) and the velocity boundary conditions in Eq. (20) are updated continuously through the simulation.

The predicted absolute rise velocities using the different reference frames are shown in Fig. 4. We note rise velocities in excellent agreement between the MRF's and the absolute reference frame. This agreement indicates that our implementation of the MRF method can handle both inertial and non-inertial reference frames consistently.

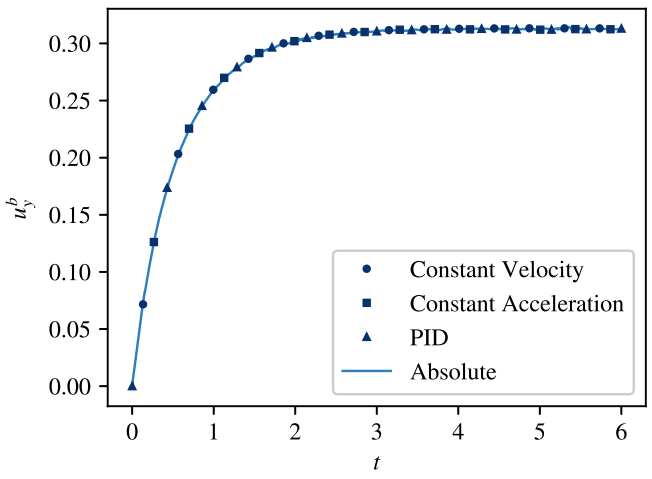

Fig. 4. Nondimensional absolute bubble rise velocities over nondimensional time in the case of a 2D bubble rising rectilinearly in a quiescent liquid. The governing parameters are $Ga = 10$ and $Eo = 1$. All of the moving reference frames predict bubble rise velocities in excellent agreement with the absolute reference frame.

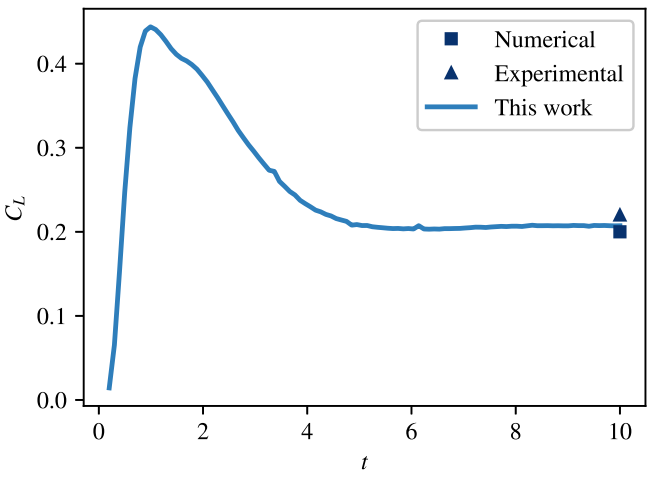

Fig. 5. Comparison between the predicted lift force coefficient using the PID-controlled MRF and the numerical study of Dijkhuizen et al. (2010) with the parameters ($Ga = 35$, $Eo = 2.5$, $Sr = 0.04$) and the experimental study by Aoyama et al. (2017) with the parameters ($Ga = 44$, $Eo = 2.25$, $Sr = 0.12$). We note a good agreement between our simulation results and the existing studies for a similar case of a bubble rising in a linear shear flow.

3.3. Lift force on a bubble rising in linear shear flow

Here, we perform a quantitative validation of the numerical method by examining the motion of a bubble in a linear shear flow using the PID-controlled MRF and compare the predicted lift force coefficient with existing experimental and numerical studies (Aoyama et al., 2017; Dijkhuizen et al., 2010). In a shear flow, the bubble obtains a preferential lateral drift direction depending on the problem parameters. Interestingly, for an air bubble in water, the lateral drift direction changes at a critical bubble diameter of about 5 mm (Tomiyama et al., 2002). In a polydisperse bubbly flow, such as in a bubble column, it is crucial to have accurate sub-grid models for the lift force to predict the spatial distribution of the bubbles (Ertekin et al., 2021).

In this validation case, the problem parameters are $Ga = 35$, $Eo = 2.4$ and the dimensionless shear rate is $Sr = -0.04$. These parameters are similar to the case studied numerically by Dijkhuizen et al. (2010). The bubble is initially placed at $x_i = 0$ and then rises in the positive y-direction due to buoyancy. The external liquid velocity profile $V_y^{(1)} = Srx$ induces a lift force on the bubble so that it migrates in the transverse x-direction. By setting up a steady-state force balance on the bubble, using the lift, drag, added mass and buoyancy forces, we can calculate the lift force coefficient. Using the same formulation of the lift force as in Tomiyama et al. (2002), the expression for the lift force coefficient is

$$C_L = -\frac{u_x^r}{(u_y^r)^2 + (u_x^r)^2}\left(\frac{1}{Sr} - \frac{u_x^r}{2}\right). \tag{30}$$

Here, we use the non-dimensional relative velocities $u_i^r = u_i^b - V_i^{(1)}$ and assume $\rho_r \gg 1$ and the added mass coefficient as $1/2$.

The computational domain is $(10D)^3$ with the bubble kept in the center of the domain using the MRF approach. To reduce the computational cost, we make use of the adaptive grid refinement technique in Basilisk with a maximum grid resolution of more than 200 cells/D.

The instantaneous lift force coefficient is computed using Eq. (30) and is shown in Fig. 5. Once the bubble reaches a steady state relative motion, the predicted lift force coefficient agrees well with existing numerical and experimental studies. This result shows that the Basilisk code with our PID-controlled MRF implementation predicts results in quantitative agreement with existing numerical and experimental data. Next, we qualitatively validate the MRF method for a multiple bubble system.

3.4. Coalescence of two bubbles

In this section we validate the ability of the PID-controlled MRF to keep the center of mass of two bubbles in the center of the computational domain and capture the bubble coalescence process. Since the bubble breakup and coalescence processes can significantly alter the bubble size distribution in bubbly flow systems, these processes need to be accurately resolved to understand the dynamics of the entire system. A demonstration case for bubble breakup in linear shear flow using our MRF method is presented in Appendix B.

According to the film drainage model, the coalescence process follows three main steps (Ozan and Jakobsen, 2019). First, the two bubbles come close to each other and trap a liquid film between them. Second, if the forces exerted by the bubbles on the liquid film are sufficiently large, the liquid film drains out and breaks, inducing coalescence. Our simulations in this section aim to showcase how the present method deals with such a bubble collision process.

We simulate two initially spherical bubbles placed $1.75D$ between their centers of mass in the vertical direction. The buoyancy force accelerates the bubbles upwards, and because of the wake of the top bubble, the bottom bubble rises faster, eventually colliding with the top bubble. The vorticity in the wake of the top bubble lowers the pressure at the rear stagnation point, thereby attracting the bottom bubble. On the other hand, a repulsive effect is generated in the gap between the bubbles where the liquid velocity reaches a minimum that induces a pressure maximum. Depending on whether or not the net attractive force from these opposing effects is large enough to drain the thin liquid film, the bubbles may either coalesce, bounce or stay in contact for a long time (Zhang et al., 2021).

We use a 2D computational domain of $20D \times 20D$ with the two bubbles close to the center of the domain. The PID-controlled MRF ensures that the center of mass of the bubbles remains in the center of the domain. The bubbles rise in a quiescent liquid, and the problem parameters are $Ga = 30$ and $Eo = 0.1$. In the VOF framework, the bubbles inherently coalesce when the bubble interfaces occupy the same computational cell. To accurately resolve the drainage of the film and to avoid premature coalescence, a high grid resolution is required in the liquid between the bubbles. For this purpose, we use the adaptive grid with a maximum refinement close to the bubble corresponding to more than 200 cells/D.

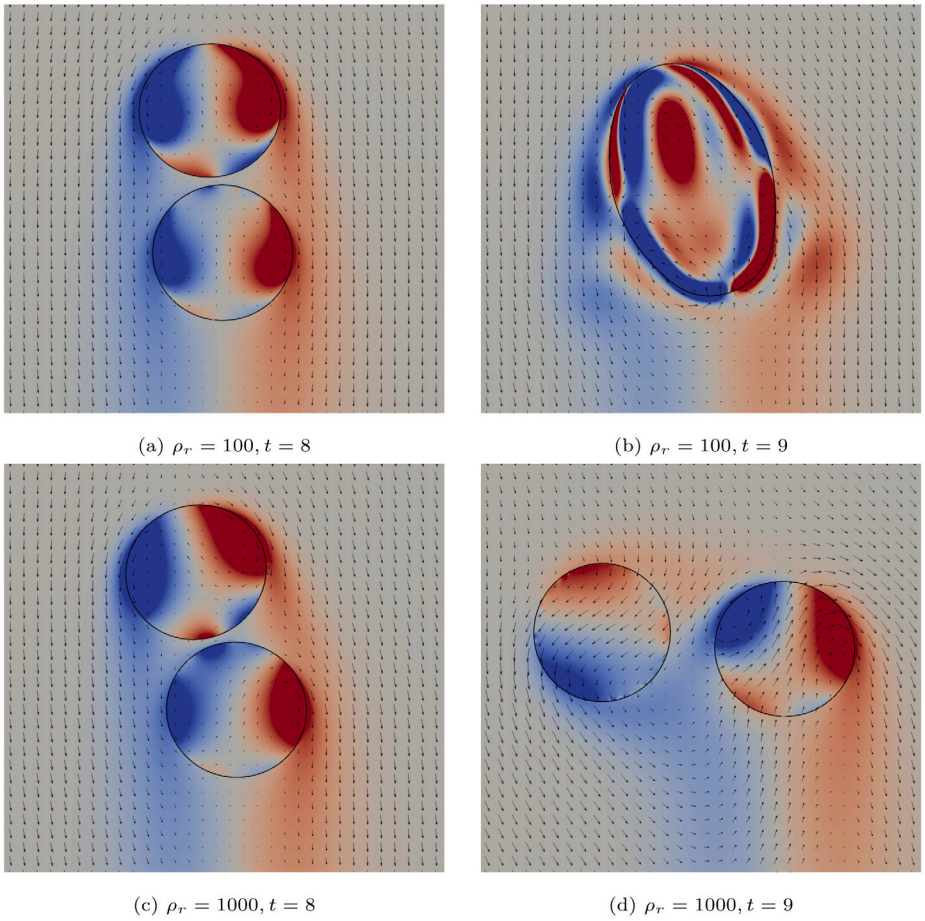

Fig. 6. Validation case for the coalescence process of two bubbles rising in a quiescent liquid using our MRF method. At a density ratio of $\rho_r = 100$ the bubbles coalesce while at $\rho_r = 1000$ there is no coalescence. The instants are taken at the non-dimensional time $t/\sqrt{D/g}$ and the governing parameters are $Ga = 30$ and $Eo = 0.1$. The coarse black line is the bubble interface, the contour levels represent the vorticity field, and the arrows illustrate the velocity field relative to the bubble's center of mass. The center of mass of the two-bubble system is kept in the center of the computational domain using the PID-controlled MRF method. Note that the subfigures do not show the full domain.

Our MRF results are validated by comparing the predicted coalescence process with the DNS results of Innocenti et al. (2021). They studied the same problem setup, at varying ρ_r, in a periodic domain and found that coalescence occurs up to a density ratio of around $\rho_r = 200$. They also found that grid independence is reached at about 200 cells/D, indicating that the thin liquid film is sufficiently resolved.

We simulate a case with $\rho_r = 100$ at which coalescence should occur and a second case with $\rho_r = 1000$ where coalescence should not occur. Instants from the simulation case with $\rho_r = 100$ are shown in Fig. 6(a-b) and for $\rho_r = 1000$ in Fig. 6(c-d).

As indicated in Fig. 6, the bubbles in both simulation cases come into contact at around $t = 8$. At this instant, the process of squeezing the thin liquid film between the bubbles starts. At $\rho_r = 100$, the net attractive force between the bubbles is sufficient to drain the liquid film between them. Consequently, at $t = 9$, the bubbles coalesce into a larger bubble that again tends to retrieve an approximately spherical shape with a minimum of interfacial energy. However, at $\rho_r = 1000$, the net attractive force is too small for the liquid film to drain, and the bubbles instead bounce apart. These results are in good qualitative agreement with the numerical study of Innocenti et al. (2021).

This validation case shows that we can capture the process of coalescence in a multiple bubble system using our MRF method. The inherent ability to follow multiple bubbles stems from Eq. (27) that determines the relative center of mass for the entire bubble phase in the computational domain. With this approach, the PID-controller can track an arbitrary number of localized bubbles without any modifications. Although this is a simple configuration, an extension to more complex systems, such as localized bubble swarms with possible coinciding breakup and coalescence processes, is straightforward due to the general methodology of the MRF method.

3.5. Bubble rising in turbulent flows

Finally, we combine the macro and microscale frameworks to simulate a rising bubble in a turbulent environment. This case represents a multiphase simulation of a bubble rising in a homogeneous isotropic turbulence. The macroscale turbulent field is the same as described in Section 3.1, while the rising bubble is characterized by $Ga = 65$ and $Eo = 10$ that corresponds to a 0.76 mm air bubble in water but with a reduced surface tension to obtain larger deformations of the bubble. The bubble is kept in the center of a $(10D)^3$ PID-controlled MRF domain with the unsteady external velocity field imposed as described in Section 3.1. The computational spatial domain is discretized using the adaptive grid refinement technique with a maximum grid resolution of more than 50 cells/D. The time step size is also variable and determined using the CFL-criterion with a Courant number of 0.5. With this setup, we resolve the small-scale bubble dynamics in response to the turbulent external velocity field obtained from the macroscale solver described in Section 2.1.

In the MRF, an initially spherical bubble is placed in the linearized velocity field $V_i^{(1)}(\hat{x_i}, t = 0)$. Then, the bubble starts to deform and to rise due to buoyancy. The external velocity field at the bubble position and its gradients are obtained at the bubble position in the macroscale simulation as $u_i^{e,b}(t) = u_i^e(x_i^b(t))$, and then imposed in the

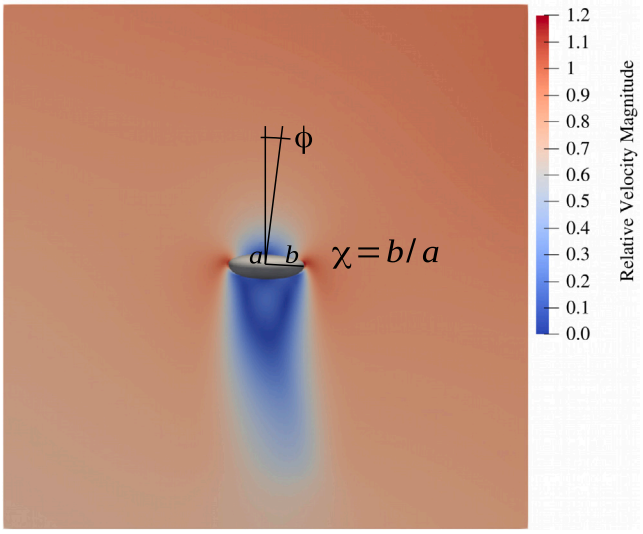

Fig. 7. Instantaneous visualization of the deformed bubble with contours representing the relative velocity magnitude in a framework moving with the bubble. The contour values have been normalized with the characteristic velocity scale $\sqrt{gD}$. The orientation angle Φ represents the angle between the bubble semi-minor axis (denoted a) and the vertical y-axis. The bubble aspect ratio χ is the ratio of the bubble semi-minor and semi-major (denoted b) axes.

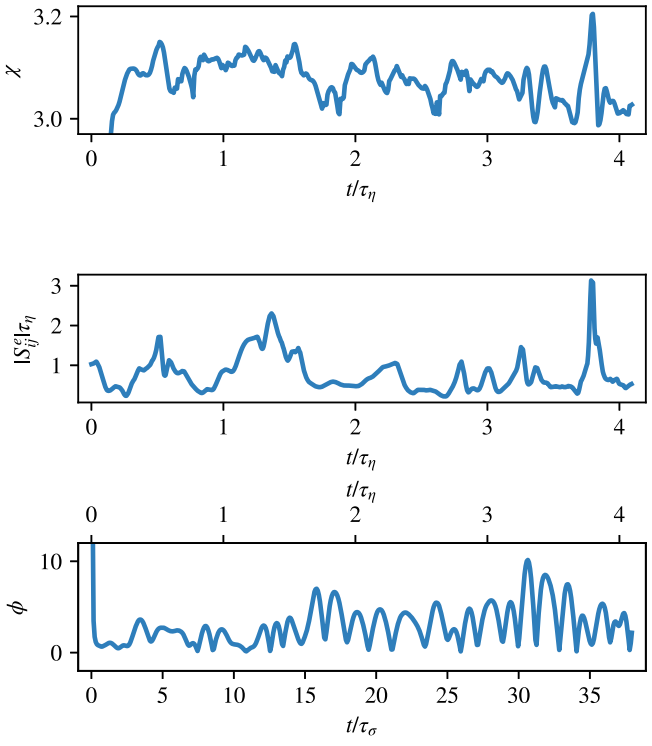

Fig. 8. Time series of the bubble aspect ratio (top panel), modulus of the external velocity field strain rate (central panel) and the bubble orientation angle (bottom panel) until around 4 Kolmogorov times. The aspect ratio and orientation angle are obtained from the microscale framework where we resolve the small-scale bubble dynamics in response to the turbulent external velocity field given by the macroscale framework. In the bottom panel, time is made non-dimensional using the capillary time scale τ_σ.

MRF domain using Eq. (21) and (22) at the same physical time t. Since the two numerical frameworks use different time step sizes, we use a linear interpolation in time to map the velocity field and its gradients from the macroscale to the microscale framework. In the current version of the numerical algorithm, the bubble trajectories in the microscale and macroscale systems are different because the equations of motion in the Eulerian–Lagrangian approach are modeled under the hypothesis of undeformable spheres and using empirical coefficients for estimating the different forces acting on the bubble. Consequently, the coupling between the two systems is one-way, with the dynamics at the macroscale affecting those at the microscale. However, we plan to extend the numerical framework by extracting the velocity and gradients from the macroscale simulation at the absolute bubble position predicted by the microscale framework if we combine the two different solvers and execute them simultaneously. The tracking of a Lagrangian bubble in the macroscale framework will be substituted by just an interpolation routine at a specific location dictated by the microscale bubble trajectory. This extension will allow a full two-way coupling between the frameworks.

An instantaneous visualization of the relative velocity field obtained by a simultaneous event of the rising bubble and turbulence is shown in Fig. 7. We note that the bubble from an initial spherical shape has an ellipsoidal configuration with an aspect ratio $\chi = b/a \simeq 3$, where b and a denote the semi-major and semi-minor axes, respectively. The contour levels show the relative velocity field normalized with the velocity scale $\sqrt{gD}$ including the wake released by the rising bubble.

To better quantify the bubble deformation dynamics, we compute the bubble aspect ratio according to the definition by Bunner and Tryggvason (2003) where χ is defined as the ratio between the larger and smaller eigenvalues, $\chi = b/a \approx (I_{max}/I_{min})^{1/2}$, of the second moment of inertia tensor

$$I_{ij} = \frac{1}{m^b}\int_{\Omega^b}(\hat{x}_i - \hat{x}_i^b)(\hat{x}_j - \hat{x}_j^b)\rho^b d\hat{V}\,, \tag{31}$$

where Ω_B is the bubble volume.

The top panel of Fig. 8 shows a time series of the bubble aspect ratio during the first 4 computational times of the simulation in Kolmogorov units. Initially, $\chi = 1$ since the bubble is spherical, but, due to the combination of the rising motion and the turbulent fluctuations, the bubble becomes ellipsoidal with a fluctuating value of the aspect ratio $\chi \approx 3$. The characteristic time scale and the intensity of the fluctuations of χ are correlated with the variation of the external turbulent velocity gradients (χ and $|S^e_{ij}|$ have a Pearson's correlation coefficient of 0.5 in the interval $t/\tau_\eta = [0.5, 4]$) by comparing with the middle panel of Fig. 8, where the time series of the macroscale rate of strain intensity is shown.

The bubble orientation angle plotted in the bottom panel of Fig. 8, however, shows a different dynamics. The orientation angle is defined as the angle between the vertical y-axis and the bubble semi-minor axis. The time series of the orientation angle is characterized by a faster dynamics compared to the smallest-scales of the turbulence, with a characteristic time much smaller than the Kolmogorov time. In particular, we note that the characteristic time scale of the orientation angle oscillation period is proportional to the capillary time scale (Popinet, 2018) $\tau_\sigma = \sqrt{\rho_l D^3/\sigma} \approx 0.1\tau_\eta$ that is an order of magnitude smaller than the Kolmogorov time. Therefore, the coupled framework can solve both the bubble deformations induced by turbulent fluctuations and the fastest dynamics due to the capillary time scale when $\tau_\sigma < \tau_\eta$.

4. Conclusions

We have formulated a numerical multiscale framework that is able to handle bubbles or droplets with arbitrary density ratios compared to the carrier phase and with diameters comparable or smaller than the Kolmogorov length scale. To take into account a high-relative velocity between the phases induced by gravity or buoyancy, we computed the equations of motion in the reference frame of the bubble (a moving reference frame). The new equations contain an additional acceleration term that was estimated using a PID controller. The numerical scheme has been validated in simple shear flows, obtaining excellent comparisons with previous numerical or experimental results. An additional body force proportional to the time derivatives of the boundary

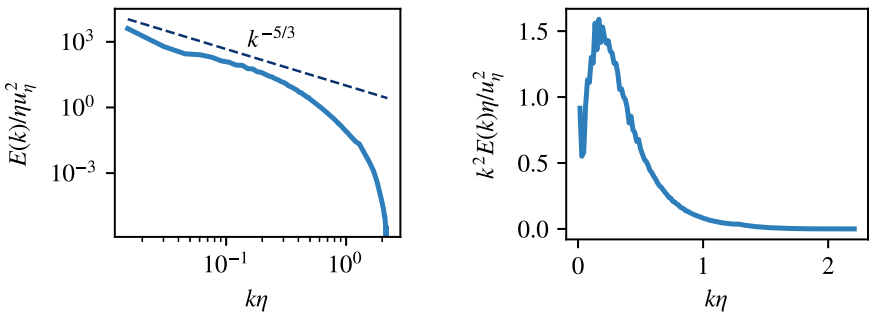

Fig. A.9. Turbulent kinetic energy (left panel) and dissipation (right panel) spectra from the pseudo-spectral simulations in Section 3.1. The values are normalized in Kolmogorov units.

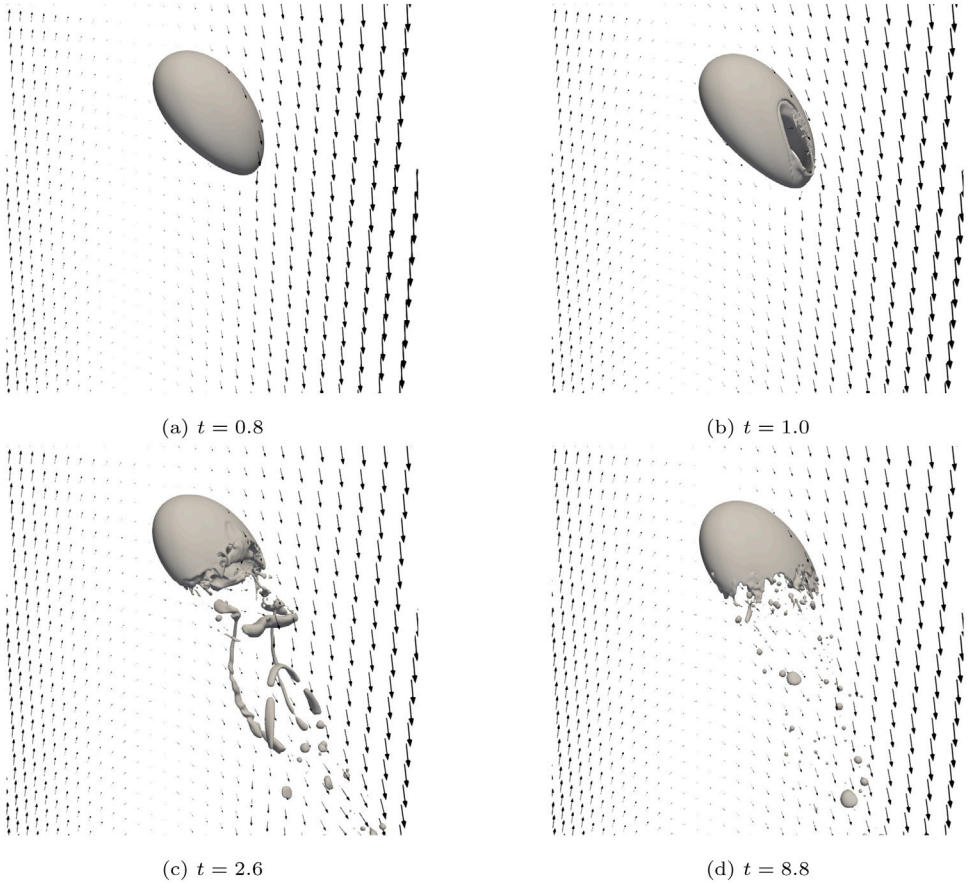

Fig. B.10. Illustration of the breakup process for a rising 3D bubble in a high shear flow. The indicated instants are the nondimensional time $t/\sqrt{D/g}$ and the governing parameters are $Ga = 1000$, $Eo = 200$ and $Sr = -1$. The black arrows show the relative velocity field. The initially spherical bubble is deformed due to the shear liquid flow and the interface ruptures at around $t = 1.0$. The breakup produces a liquid jet that penetrates the bubble and results in the generation of satellite bubbles.

conditions improves the efficiency of the algorithm (at least two orders of magnitudes) compared to the framework suggested by Milan et al. (2020). The novel methodology can resolve both large-scale effects induced by turbulent properties and small-scale phenomenologies induced by surface tension. In particular, we have found that the characteristic time of the bubble orientation angle (and therefore the bubble trajectory) corresponds to the capillary time scale $\tau_\sigma = \sqrt{\rho_l D^3/\sigma}$ that for highly deformable particles (low surface tension) can be smaller than the Kolmogorov time scale. The proposed algorithm has been presented in a general way, and it can be applied to any DNS technique that handles two-phase flows (VOF, level-set, lattice-Boltzmann, diffuse interface approach).

It would be interesting, as future work, to investigate the statistics of deformation and orientation angle with bubbles/droplets at different Ga and Eo numbers and different density ratios. Moreover, the current framework can be further improved by matching and running in parallel the two multiscale codes such that the turbulent external velocity and gradients in the macroscale simulation are directly calculated along the object trajectory predicted by the microscale framework. The extension will allow a full multiscale two-way coupling between the small scales of the deformable objects and the properties of the turbulent field.

CRediT authorship contribution statement

Niklas Hidman: Conceptualization, Methodology, Software, Validation, Formal analysis, Investigation, Writing – original draft, Visualization. **Henrik Ström:** Conceptualization, Supervision, Writing – review & editing. **Srdjan Sasic:** Conceptualization, Supervision, Writing

– review & editing. **Gaetano Sardina:** Conceptualization, Methodology, Software, Investigation, Formal analysis, Supervision, Writing – original draft, Resources, Project administration, Funding acquisition.

Declaration of competing interest

The authors declare that they have no known competing financial interests or personal relationships that could have appeared to influence the work reported in this paper.

Acknowledgments

This work was supported by the Swedish Research Council (Vetenskapsrådet), grant VR 2017-05031. The computations were enabled by resources provided by the Swedish National Infrastructure for Computing (SNIC) at NSC partially funded by the Swedish Research Council through grant agreement no. 2018-05973. We would like to thank Alessio Innocenti and Sergio Chibbaro for sharing the original Basilisk input files for the validation of the coalescence cases.

Appendix A. Single-phase turbulent spectra

The turbulent kinetic energy (left panel) and dissipation spectra (right panel) are shown in Fig. A.9. The turbulent kinetic energy spectrum (left panel) shows the classic $-5/3$ power-law in the inertial range and the exponential viscous closure at high-wave numbers corresponding to the properties of a fully homogeneous isotropic turbulent flow. For our simulations, it is fundamental to be able to solve and correctly estimate the velocity gradients. The quality of the resolution when solving the turbulent gradients can be easily checked by looking at the content of the dissipation spectrum in the right panel of Fig. A.9. Because the dissipation spectrum is negligible at the smallest scales ($k\eta > 1$), we argue that the velocity gradients are well-resolved in our simulation.

Appendix B. Bubble breakup in a linear shear flow

We demonstrate the capability of the MRF approach to study the breakup process of a 3D bubble in a linear shear flow $V_y^{(1)} = Srx$. The bubble breakup occurs when the dynamic pressure difference on opposite sides of the bubble exceeds the bubble capillary pressure (Kolmogorov, 1949). In a shear flow, the relative velocity between the bubble and the liquid phase varies across the bubble interface. These differences induce variations of the dynamic pressure that can lead to the bubble breakup.

In this case, the problem parameters are $Ga = 1000$, $Eo = 200$ and $Sr = -1$ that represent a system with relatively high shear, high inertial and low surface tension forces. These force ratios are favorable for the bubble breakup to occur. Initially, a spherical bubble is placed in the center of the $(10D)^3$ domain. Here, we use a maximum grid refinement corresponding to more than 100 cells/D.

Four instantaneous visualizations that illustrate the breakup process are shown in Fig. B.10. Initially, the bubble is spherical, but due to the shear flow, it becomes almost elliptical at around $t = 0.5$. The bubble shape is increasingly elongated until the bubble interface, due to the high relative liquid velocity, ruptures at around $t = 1.0$. The rupture induces, due to surface tension, a liquid jet that penetrates the main bubble. At around $t = 2.6$, the elongated part of the bubble has collapsed, and this process continues beyond $t = 8.8$.

This case shows that the PID-controlled MRF can capture the bubble breakup process and track the resulting multiple bubbles.

References

Aoyama, S., Hayashi, K., Hosokawa, S., Lucas, D., Tomiyama, A., 2017. Lift force acting on single bubbles in linear shear flows. Int. J. Multiph. Flow 96, 113–122.
Balachandar, S., Liu, K., Lakhote, M., 2019. Self-induced velocity correction for improved drag estimation in Euler–Lagrange point-particle simulations. J. Comput. Phys. 376, 160–185.
Bunner, B., Tryggvason, G., 1999. Direct numerical simulations of three-dimensional bubbly flows. Phys. Fluids 11 (8), 1967–1969.
Bunner, B., Tryggvason, G., 2003. Effect of bubble deformation on the properties of bubbly flows. J. Fluid Mech. 495, 77.
Cano-Lozano, J.C., Martinez-Bazan, C., Magnaudet, J., Tchoufag, J., 2016. Paths and wakes of deformable nearly spheroidal rising bubbles close to the transition to path instability. Phys. Rev. Fluids 1 (5), 053604.
Conesa, J.A., 2019. Chemical Reactor Design: Mathematical Modeling And Applications. John Wiley & Sons.
Delnoij, E., Kuipers, J., van Swaaij, W.P.M., 1999. A three-dimensional CFD model for gas–liquid bubble columns. Chem. Eng. Sci. 54 (13–14), 2217–2226.
Dijkhuizen, W., van Sint Annaland, M., Kuipers, J., 2010. Numerical and experimental investigation of the lift force on single bubbles. Chem. Eng. Sci. 65 (3), 1274–1287.
Ertekin, E., Kavanagh, J.M., Fletcher, D.F., McClure, D.D., 2021. Validation studies to assist in the development of scale and system independent CFD models for industrial bubble columns. Chem. Eng. Res. Des. 171, 1–12.
Evrard, F., Denner, F., van Wachem, B., 2020. Euler-Lagrange modelling of dilute particle-laden flows with arbitrary particle-size to mesh-spacing ratio. J. Comput. Phys.: X 8, 100078.
Fan, Y., Fang, J., Bolotnov, I., 2021. Complex bubble deformation and break-up dynamics studies using interface capturing approach. Exp. Comput. Multiph. Flow 3 (3), 139–151.
Ferrante, A., Elghobashi, S., 2004. On the physical mechanisms of drag reduction in a spatially developing turbulent boundary layer laden with microbubbles. J. Fluid Mech. 503, 345–355.
Gualtieri, P., Picano, F., Sardina, G., Casciola, C.M., 2015. Exact regularized point particle method for multiphase flows in the two-way coupling regime. J. Fluid Mech. 773, 520–561.
van der Hoef, M.A., van Sint Annaland, M., Deen, N., Kuipers, J., 2008. Numerical simulation of dense gas-solid fluidized beds: a multiscale modeling strategy. Annu. Rev. Fluid Mech. 40, 47–70.
Horwitz, J., Mani, A., 2018. Correction scheme for point-particle models applied to a nonlinear drag law in simulations of particle-fluid interaction. Int. J. Multiph. Flow 101, 74–84.
Innocenti, A., Jaccod, A., Popinet, S., Chibbaro, S., 2021. Direct numerical simulation of bubble-induced turbulence. J. Fluid Mech. 918, A23.
Jareteg, K., Ström, H., Sasic, S., Demazière, C., 2017. On the dynamics of instabilities in two-fluid models for bubbly flows. Chem. Eng. Sci. 170, 184–194.
Kekesi, T., Amberg, G., Wittberg, L.P., 2016. Drop deformation and breakup in flows with shear. Chem. Eng. Sci. 140, 319–329.
Kolmogorov, A., 1949. On the disintegration of drops in a turbulent flow. In: Dokl. Akad. Nauk SSSR. 66, (825–828), p. 30.
Lörstad, D., Francois, M., Shyy, W., Fuchs, L., 2004. Assessment of volume of fluid and immersed boundary methods for droplet computations. Int. J. Numer. Methods Fluids 46 (2), 109–125.
Lörstad, D., Fuchs, L., 2004. High-order surface tension VOF-model for 3D bubble flows with high density ratio. J. Comput. Phys. 200 (1), 153–176.
Magnaudet, J., Eames, I., 2000. The motion of high-Reynolds-number bubbles in inhomogeneous flows. Annu. Rev. Fluid Mech. 32 (1), 659–708.
Maxey, M.R., Riley, J.J., 1983. Equation of motion for a small rigid sphere in a nonuniform flow. Phys. Fluids 26 (4), 883–889.
McCormack, A.S., Godfrey, K.R., 1998. Rule-based autotuning based on frequency domain identification. IEEE Trans. Control Syst. Technol. 6 (1), 43–61.
Mei, R., Klausner, J.F., 1992. Unsteady force on a spherical bubble at finite Reynolds number with small fluctuations in the free-stream velocity. Phys. Fluids A: Fluid Dyn. 4 (1), 63–70.
Milan, F., Biferale, L., Sbragaglia, M., Toschi, F., 2020. Sub-Kolmogorov droplet dynamics in isotropic turbulence using a multiscale lattice Boltzmann scheme. J. Comput. Sci. 45, 101178.
Ozan, S.C., Jakobsen, H.A., 2019. On the role of the surface rheology in film drainage between fluid particles. Int. J. Multiph. Flow 120, 103103.
Panicker, N., Passalacqua, A., Fox, R.O., 2020. Computational study of buoyancy driven turbulence in statistically homogeneous bubbly flows. Chem. Eng. Sci. 216, 115546.
Pope, S.B., 2001. Turbulent Flows. IOP Publishing.
Popinet, S., 2003. Gerris: a tree-based adaptive solver for the incompressible Euler equations in complex geometries. J. Comput. Phys. 190 (2), 572–600.
Popinet, S., 2015. A quadtree-adaptive multigrid solver for the Serre–Green–Naghdi equations. J. Comput. Phys. 302, 336–358.
Popinet, S., 2018. Numerical models of surface tension. Annu. Rev. Fluid Mech. 50, 49–75.
Rusche, H., 2002. Computational fluid dynamics of dispersed two-phase flows at high phase fractions. (Ph.D. thesis). University of London.

Sardina, G., Jareteg, K., Ström, H., Sasic, S., 2019. Assessing the ability of the Eulerian-Eulerian and the Eulerian-Lagrangian frameworks to capture meso-scale dynamics in bubbly flows. Chem. Eng. Sci. 201, 58–73.

Sardina, G., Picano, F., Brandt, L., Caballero, R., 2015. Continuous growth of droplet size variance due to condensation in turbulent clouds. Phys. Rev. Lett. 115 (18), 184501.

Scardovelli, R., Zaleski, S., 1999. Direct numerical simulation of free-surface and interfacial flow. Annu. Rev. Fluid Mech. 31 (1), 567–603.

Spandan, V., Ostilla-Mónico, R., Verzicco, R., Lohse, D., 2016. Drag reduction in numerical two-phase Taylor–Couette turbulence using an Euler–Lagrange approach. J. Fluid Mech. 798, 411–435.

Tomiyama, A., Tamai, H., Zun, I., Hosokawa, S., 2002. Transverse migration of single bubbles in simple shear flows. Chem. Eng. Sci. 57 (11), 1849–1858.

Toschi, F., Bodenschatz, E., 2009. Lagrangian properties of particles in turbulence. Annu. Rev. Fluid Mech. 41, 375–404.

Tripathi, M.K., Sahu, K.C., Govindarajan, R., 2014. Why a falling drop does not in general behave like a rising bubble. Sci. Rep. 4, 4771.

Tryggvason, G., Scardovelli, R., Zaleski, S., 2011. Direct numerical simulations of gas–liquid multiphase flows. Cambridge University Press.

Zhang, J., Ni, M.-J., Magnaudet, J., 2021. Three-dimensional dynamics of a pair of deformable bubbles rising initially in line. Part 1. Moderately inertial regimes. J. Fluid Mech. 920.

Ziegler, J.G., Nichols, N.B., et al., 1942. Optimum settings for automatic controllers. Trans. ASME 64, 11.